RSC Advances

PAPER

View Article Online
View Journal | View Issue

Cite this: *RSC Adv.*, 2017, **7**, 13985

Tailoring of enhanced interfacial polarization in WO_3 nanorods grown over reduced graphene oxide synthesized by a one-step hydrothermal method

Bilal Ahmed,[a] Animesh K. Ojha,*[a] Florian Hirsch,[b] Ingo Fischer,[b] Donfack Patrice[c] and Arnulf Materny[c]

In the present report, well-defined WO_3 nanorods (NRs) and a rGO–WO_3 composite were successfully synthesized using a one-pot hydrothermal method. The crystal phase, structural morphology, shape, and size of the as-synthesized samples were studied using X-ray diffraction (XRD) and transmission electron microscopy (TEM) measurements. The optical properties of the synthesized samples were investigated by Raman, ultraviolet-visible (UV-Vis) and photoluminescence (PL) spectroscopy. Raman spectroscopy and TEM results validate the formation of WO_3 (NRs) on the rGO sheet. The value of the dielectric constant (ε') of WO_3 NRs and rGO–WO_3 composite is decreased with an increase in frequency. At low frequency (2.5 to 3.5 Hz), the value of ε' for the rGO–WO_3 composite is greater than that of pure WO_3 NRs. This could be due to the fact that the induced charges follow the ac signal. However, at higher frequency (3.4 to 6.0), the value of ε' for the rGO–WO_3 composite is less compared to that of the pure WO_3 NRs. The overall decrease in the value of ε' could be due to the occurrence of a polarization process at the interface of the rGO sheet and WO_3 NRs. Enhanced interfacial polarization in the rGO–WO_3 composite is observed, which may be attributed to the presence of polar functional groups on the rGO sheet. These functional groups trap charge carriers at the interface, resulting in an enhancement of the interfacial polarization. The value of the dielectric modulus is also calculated to further confirm this enhancement. The values of the ac conductivity of the WO_3 NRs and rGO–WO_3 composite were calculated as a function of the frequency. The greater value of the ac conductivity in the rGO–WO_3 composite compared to that of the WO_3 NRs confirms the restoration of the sp^2 network during the *in situ* synthesis of the rGO–WO_3 composite, which is well supported by the results obtained by Raman spectroscopy.

Received 17th January 2017
Accepted 19th February 2017

DOI: 10.1039/c7ra00730b

rsc.li/rsc-advances

1. Introduction

Dielectric materials are capable of storing electrical energy. They are important for electronics, particularly in making devices such as capacitors, electronic switches, resonators, *etc.*[1] The material parameters used to design efficient and miniaturized devices are high dielectric constant (ε') and low dielectric loss (ε'').[2] Therefore, the synthesis of such materials has been the subject of immense research interest for the scientific community. The composite materials such as metal oxides grown over graphene are known to have a high dielectric constant and low dielectric loss along with the improved interfacial interaction between the graphene layers and metal oxide nanostructures.[2–4] Metal oxides and carbon-based materials are used for the synthesis of composite materials, among which graphene and its derivatives play an important role in modifying the various properties of the composite.[5]

Graphene-based composites with high dielectric constant have potential application in the field of anti-static, electromagnetic interference shielding, electronic and electro-mechanical systems such as super capacitors, dielectric actuators, rechargeable batteries and energy storage devices.[6,7] Various metal oxides and graphene-based nanocomposites have been synthesized to obtain high dielectric constant.[4,5] Graphene oxide (GO) is often synthesized through oxidation of natural graphite by different methods.[8,9] Reduced graphene oxide (rGO) is another allotrope of carbon having two-dimensional single atomic layers. Graphene possesses a unique two-dimensional structure with sp^2-hybridized carbon atoms and having unique properties. It shows remarkable properties such as large surface area, good electrical conductivity, and high flexibility.[9,10] The rGO sheets also offer an excellent electronic conductivity based on their two-dimensional

[a]*Department of Physics, Motilal Nehru National Institute of Technology, Allahabad-211004, India. E-mail: animesh@mnnit.ac.in; animesh198@gmail.com; Fax: +91-532-227-2545341; Tel: +91-532-2271289*

[b]*Institute of Physical and Theoretical Chemistry, University of Wuerzburg, Am-Hubland, D-97074, Germany*

[c]*Department of Physics and Earth Sciences, Jacobs University Bremen, Campus Ring 1, 28759 Bremen, Germany*

planar pie-(π)-conjugation structure. Graphene acts as a superior supporting matrix for the binding of various functional components. Recently, a number of ceramic, metal, and polymer-based composites have been studied due to their easy processing, flexibility and high dielectric strength.[11] Considerable, efforts have also been made to explore various properties of graphene-based metal oxide (*e.g.* TiO_2, MnO_2, InO, ZnO, CuO_2, MoO_3, CdO and WO_3) composites.[12–15]

Tungsten oxide (WO_3) is a transition metal oxide which exists in the WO_2 and WO_3 structural forms. WO_3 is an n-type semiconductor with a narrow band gap (E_g = 2.4–2.8 eV) and refractive index of ~1.[16] It is also one of the most important materials due to its high physical and chemical stability.[17,18] It has been used in gas sensors, solar devices, electrode materials for secondary batteries, and field emission devices.[19–22] Recently, Wu *et al.*[4] have synthesized chlorine-doped graphene-based poly-vinylidene fluoride nanocomposites *via* the sol–gel method. Several reports can be found in the literature on graphene-polymer, and graphene-metal oxide composites.[5–7]

In view of the above discussed studies and applications of rGO–metal oxide composites, there has been a study of the dielectric behaviour of WO_3.[23] However, to the best of our knowledge, the studies on dielectric properties of WO_3 NRs grown over rGO sheets have not yet been done. Motivated by the unique electrical and optical properties of graphene and differently shaped WO_3 nanostructures, as described above, we planned to synthesize rGO–WO_3 (NRs) composites using a simple and low-cost synthesis method. The structural and optical properties of as synthesized products are investigated by X-ray diffraction (XRD), transmission electron microscopy (TEM), Raman, photoluminescence (PL), and ultra-violet visible (UV-Vis) absorption measurements. Due to the presence of localized electrons on the surface of graphene, the polarization of the electronic charge of WO_3 NRs grown over the rGO sheets is expected to modify compared to that of the pure WO_3 NRs. As a result, the dielectric behaviour of WO_3 NRs should vary at the interface. Thus, in the present report, the influence of metal oxide and rGO interface on dielectric properties such as, permittivity, tangent loss, AC conductivity, and interfacial polarization of rGO–WO_3 composites have also been studied systematically as function of the applied field. The composite material synthesized herein can widely be applied to manufacture charge storage capacitors in future.

2. Experimental details

2.1. Materials

High quality graphite flakes of 7–10 microns in size, as well as $KMnO_4$, $Na_2WO_4 \cdot 2H_2O$, NaCl, H_2SO_4, H_3PO_4, H_2O_2, HCl, C_2H_5OH and N_2H_4 chemicals were purchased from Alfa Aesar. All the chemicals were of analytical grade and used without any further purification. The solutions were prepared in Milli-Q water.

2.2. Synthesis of GO

The GO was synthesized using a modified Hummer's methods[8] with some modifications. Briefly, a 9 : 1 mixture of concentrated H_2SO_4 and H_3PO_4 (360 : 40 ml) was prepared in a conical flask. 6 g expandable graphite flakes were mixed into the mixture of concentrated H_2SO_4 and H_3PO_4. The mixture was then stirred for 30 min. Thereafter, 18 g $KMnO_4$ was added slowly to this solution under vigorous stirring at a temperature lying in the range of 35–40 °C. During the oxidation reaction, the color of the solution changed to dark brown. The reaction was then heated to 50 °C and stirred further for 10 to 12 h to complete the oxidation of graphite. The reaction product was allowed to cool at room temperature. The chemical reaction was terminated by adding ice (400 ml) with 30% H_2O_2 solution. The color of the solution changed to bright yellow, indicating the oxidation of graphite. The obtained solution was centrifuged at 2500 rpm. The collected precipitate was then washed with Milli-Q water, 30% HCl and C_2H_5OH in a successive order until the pH of the solution reached a value of 5. Thereafter, the solution was dried overnight at 40 °C. The obtained powder of GO was collected and used for the investigations.

2.3. Synthesis of rGO

rGO was synthesized by a facile one-pot *in situ* solvo-thermal method. For the synthesis of rGO, 0.04 g of as synthesized powder was first dispersed into 40 ml of milli-Q distilled water at room temperature. The dispersed GO was then exfoliated under ultra-sonication treatment for 1 h and subsequently, 10 μl of N_2H_4 was added drop-wise in the solution under ultra-sonication. The solution was transferred into a 50 ml Teflon-lined stainless steel autoclave and heated at 160 °C for 12 h. The autoclave was then cooled to room temperature. The obtained precipitate was washed with milli-Q water and C_2H_5OH. The remaining material was then dried at 60 °C in an open air oven. Black powder of rGO was collected as final product for further use.

2.4. Synthesis of WO_3 nanorods

WO_3 NRs were synthesized using a hydrothermal process with NaCl as a capping agent. For the synthesis, 0.25 M $Na_2WO_4 \cdot 2H_2O$ was used as the tungsten source and dissolved into 40 ml of milli-Q distilled water. The pH value of the Na_2WO_4 solution was found to be ~8. A white precipitate appeared when excess HCl was added into the solution to reduce the pH of the solution to 2. Further, 1.5 g of NaCl was added to the solution under vigorous stirring. The resultant solution was then kept for further stirring for 2 h. Thereafter, the solution was transferred to a 50 ml Teflon-lined stainless steel autoclave and heated at 160 °C for 12 h. The stainless steel autoclave was then allowed to cool at room temperature. The precipitate thus obtained was separated through centrifugation and washed with milli-Q distilled water and absolute alcohol until the value of pH reached to 5. The remaining sample was dried at 60 °C. The obtained powder was then analyzed using different characterization techniques.

2.5. Synthesis of WO_3 nanorods over the rGO

A one-step *in situ* solvo-thermal method was used to synthesize WO_3 NRs over the rGO sheet. In brief, a small amount of GO

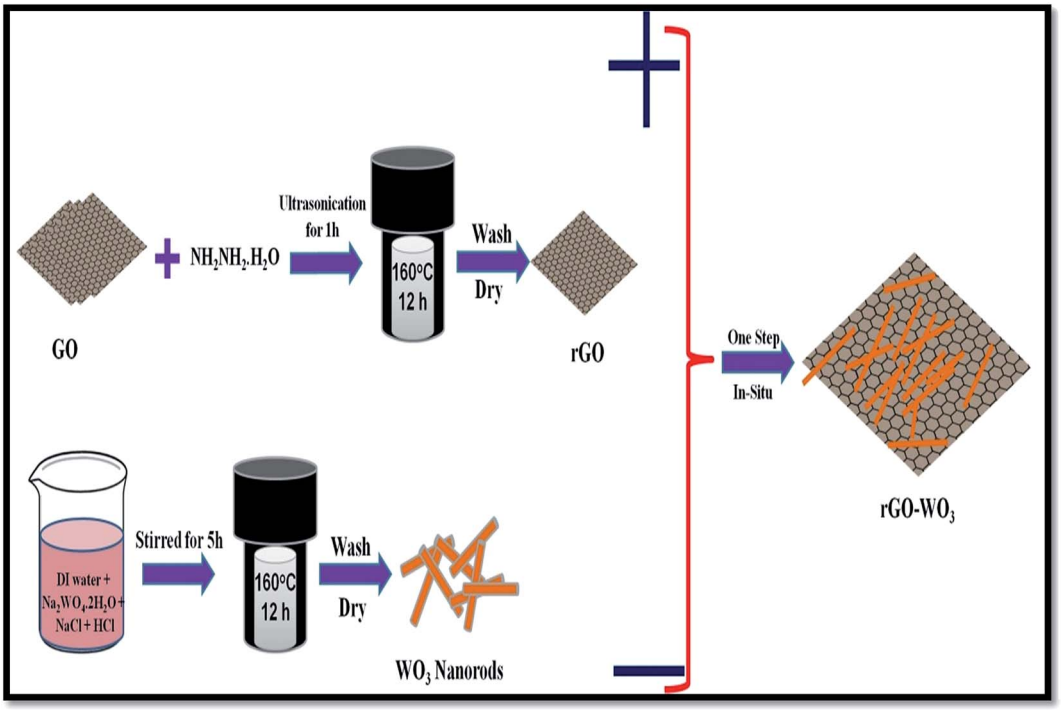

Fig. 1 Schematic of synthesis steps used for the synthesis of WO_3 NRs and rGO–WO_3 composite.

(0.04 g) was added to 40 ml of milli-Q distilled water and the mixture was sonicated until the GO was completely dispersed in the aqueous solution. Then 100 μl of N_2H_4 was added drop wise into the solution under ultra-sonication treatment. Further, 0.25 M of $Na_2WO_4 \cdot 2H_2O$ was added into that solution under vigorous stirring. The pH value of the Na_2WO_4 solution was found to be ~8. An excess amount of HCl was added into the solution to reduce the pH of the solution to 2, which results a white precipitate. Thereafter, 1.5 g of NaCl was added into the prepared solution. The resultant solution was then kept for further stirring for 2 h. Thereafter, the solution was transferred into a 50 ml Teflon-lined stainless steel autoclave and heated at 160 °C for 12 h. The autoclave was then cooled to room temperature and the precipitate was collected through centrifugation. The obtained precipitate was washed with milli-Q distilled water and absolute alcohol several times until the pH of the solution reached a value of 5. Finally, the precipitate was collected and dried in an open air oven at 60 °C. The addition of extra amount of HCl controls the nucleation of WO_3 NRs over the rGO sheet. The obtained powder was then characterized using different techniques. A schematic of the synthesis steps used in the present study is shown in Fig. 1.

3. Characterization techniques

The structure and crystalline phase of the synthesized samples were characterized by XRD (Rigaku smart lab X-ray diffractometer) using the CuK_α radiation ($\lambda = 0.154$ nm). XRD spectra were recorded for the 2θ values ranging from 5 to 40°. The structural morphology, shape, and size of the nanostructured samples were studied using a TEM (JEOL JEM 2100). The operating accelerating voltage was kept to 200 kV. An electron diffraction pattern was also taken to ascertain the crystallinity of the samples. Raman spectroscopy measurements were performed at room temperature using a Renishaw invia Raman spectrometer. The Raman spectra of the samples were recorded in the spectral range 1000–1800 cm^{-1} for GO and rGO, and in the range of 200–2000 cm^{-1} for WO_3 NRs and rGO–WO_3 composite with an excitation wavelength of 514.5 nm provided by an Ar ion laser with a power of ~5 mW at the sample. The optical absorption measurements were done on a Shimadzu UV-2330 spectrophotometer with one quartz cell in the spectral range of 280–620 nm. PL spectra of all the samples were also recorded at different excitation wavelengths (250, 270, and 280 nm) in the spectral range 280–480 nm using an Agilent fluorescence spectrophotometer at room temperature with a Xenon lamp as the excitation light source. Pure WO_3 NRs and rGO–WO_3 composite were compacted separately in the form of pellets of 10 mm diameter and 2.0–2.5 mm thickness under an uniaxial pressure of ~1 MPa using a hydraulic pressing unit. Both faces of the pellets were coated with an electrode of colloidal silver. For the dielectric measurement, the pellet was mounted in a specially fabricated cell, which was fixed co-axially inside a resistance unit. The broad band dielectric measurement was done using a precision impedance analyzer (Hioki LCR meter). The modulus of complex impedance ($|Z(\omega)|$) and phase angle ($\omega(\theta)$) were measured in the frequency (ω) range 100 Hz to 1 MHz at room temperature. These data were used to calculate the value of complex permittivity $\varepsilon(\omega) = \varepsilon'(\omega) - i\varepsilon''(\omega)$ as a function of the applied frequency.

4. Results and discussion

4.1. XRD

XRD measurements were done to study the structural and crystal phases of the synthesized samples. The XRD patterns of as synthesized products were recorded for 2θ values lying in the range, 5–40°. The recorded XRD spectra of the samples are shown in Fig. 2(a–d). Fig. 2(a) revealed a sharp diffraction peak centered at 10.48°, which corresponds to reflection from the (001) plane of GO. It indicates that the graphite was successfully oxidized into GO. Fig. 2(b) shows a broad diffraction peak centered at 24.57° corresponding to reflection from the (002) plane of rGO. It means that after hydrothermal treatment of GO with N_2H_4, it is reduced to few layers of rGO sheets with a relatively small number of attached functional groups (–OH, C=O, –COOH and CHO) compared to GO. The value of d spacing of the sheets is calculated to be 0.73 nm. The value of the d spacing in rGO is much greater than that of graphite (~0.36 nm). It confirms that the rGO is composed of only few layers. The value of the d spacing corresponding to the diffraction peak positioned at 24.57° turns out to be ~0.36 nm. It is greater than the theoretical value of d spacing (~0.34 nm) of graphene. It implies that the GO is not completely reduced into rGO and still few oxygen containing functional groups are present in the rGO sheet.[24] It was reported previously[8] that N_2H_4 acts as reducing agent for transforming GO into rGO. The broad peak in the rGO pattern indicates that GO was moderately reduced by N_2H_4 and exfoliated significantly. Fig. 2(c) exhibits diffraction peaks at 2θ = 20.45°, 22.82°, 27.03°, 28.18° and 35.78°, which correspond to reflections from the (140), (520), (221), (131), and (621) crystal planes of the orthorhombic crystal phase of WO_3 (JCPDS no. 81-1172), respectively. The intensity of the diffraction peaks positioned at 27.03° and 28.18° is almost the same, indicating that the growth of WO_3 nanostructures takes place preferably along these two directions. Fig. 2(d) presents the diffraction pattern of the powder sample synthesized *in situ* by mixing the GO and WO_3 based precursors. Fig. 2(d) shows diffraction peaks positioned at 13.77, 23.32, 27.81, 33.80, and 36.66°, which correspond to reflections from the (320), (001), (720), (621), and (641) crystal planes of tetragonal structures of WO_3 (JCPDS no. 71-0292), respectively. The diffraction peaks confirm the formation of the tetragonal crystalline phase of WO_3 grown over the rGO sheet. The change of crystalline phase from orthorhombic to tetragonal phase of WO_3 NRs grown over rGO sheet could be mainly due to the restructuring of WO_3 NRs causes owing to the interaction of functional groups attached with the rGO sheet. Here, we would like to add that during the synthesis process GO cannot be fully reduced into rGO and therefore some of the oxygen based functional groups are often attached to the rGO sheet even after the reduction. The interaction of these functional groups provides additional stability to the WO_3 NRs for acquiring tetragonal phase, which is absent in pure WO_3 NRs. Here, we would like to note that we could not observe any signature of rGO in the XRD pattern of rGO–WO_3 composite. This further indicates that the rGO is constituted by only few layers (five to six) of rGO sheets.

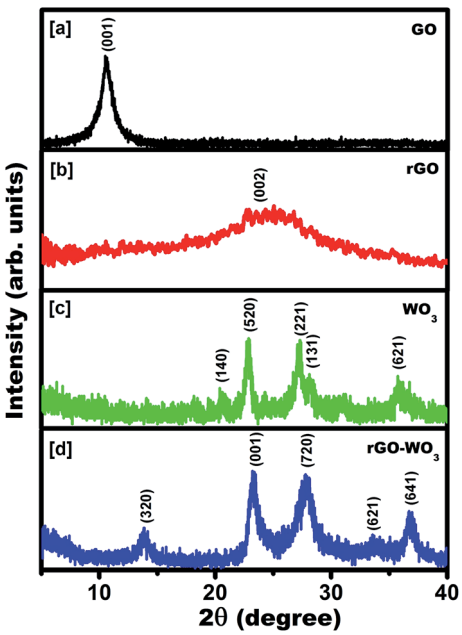

Fig. 2 XRD pattern of GO [a], rGO [b], WO_3 NRs [c], and rGO–WO_3 composite [d] composite.

The values of lattice parameters (a, b, and c) of WO_3 NRs and rGO–WO_3 composite have been calculated using the following relationship:

For orthorhombic structure:

$$\frac{1}{d^2} = \frac{h^2}{a^2} + \frac{k^2}{b^2} + \frac{l^2}{c^2}$$

For tetragonal structure:

$$\frac{1}{d^2} = \frac{h^2 + k^2}{a^2} + \frac{l^2}{c^2}$$

The lattice strain (ε) of WO_3 NRs is calculated by using the following expression:

Table 1 Calculated values of lattice constants, lattice strain, and d spacing of pure WO_3 NRs and rGO–WO_3 composite

Calculated parameters	Pure WO_3 nanorods	rGO–WO_3 composite
Phase	Orthorhombic	Tetragonal
Lattice parameters	a = 21.85 Å, b = 18.82 Å, c = 3.72 Å	a = 22.91 Å, b = 22.91 Å, c = 3.92 Å
Lattice strain	0.031	0.053
Inter-planar spacing, d	4.34 Å for (140) plane	6.43 Å for (320) plane 3.20 Å for (001) plane

$$\varepsilon = \frac{\beta}{4 \tan \theta}$$

where β, and θ are the full width at half maximum (FWHM) and Bragg's angle, respectively. The values of lattice constants, lattice strain and the d spacing calculated using the above expressions are listed in Table 1.

4.2. TEM

The structural morphology, shapes and sizes of the as prepared rGO, WO_3, and rGO–WO_3 composite are examined by analyzing the TEM micrographs shown in Fig. 3(a–c). Two-dimensional (2D) layer-like structure of rGO sheets with corrugated, curled, and wrinkled structures are observed (see Fig. 3[a(i and ii)]). The high transparency of rGO sheets reveals that the thickness of rGO layers is limited to few layers only. Fig. 3(a)(iii) shows the selected area electron diffraction (SAED) pattern of rGO. The circular ring in the SAED pattern of rGO corresponds to diffraction from the (002) plane. It also indicates that GO has been reduced to rGO with few layers of rGO sheets. Fig. 3(b)(i) revealed a rod-type structure of WO_3. A high resolution TEM image of WO_3 NRs is shown in Fig. 3(b)(ii) wherein lattice planes can easily be seen. Using Fig. 3(ii), the value of the d spacing is calculated to be 4.25 Å corresponding to the (140) plane, which also confirms the orthorhombic crystalline phase of WO_3 NRs. The SAED pattern, as shown in Fig. 3(b)(iii), shows two circular rings corresponding to diffraction from the (221) and (140) reflection planes of the orthorhombic phase of WO_3. Fig. 3(c)(i) display the TEM image of rGO–WO_3 composite (WO_3 NRs grown over rGO). A high-resolution TEM image of rGO–WO_3 composite is shown in Fig. 3(c)(ii) wherein lattice planes corresponding to the (320) and (001) planes can also be seen. With the help of Fig. 3(c)(ii), the values of the d spacing are estimated to be 7.58 Å and 3.39 Å corresponding to the (320) and (001) planes, respectively of the tetragonal phase of WO_3 grown over the rGO sheet. The values of the d spacing corresponding to WO_3 and rGO in the high resolution images of rGO–WO_3 also confirm that the WO_3 NRs are nicely grown over the rGO sheets. The TEM images also revealed that WO_3 NRs is nicely distributed over the rGO sheet (see Fig. 3(c)(i)). The crystalline structure of WO_3 NRs grown over the rGO sheet is changed to a tetragonal phase compared to the orthorhombic phase of pure WO_3 NRs, indicating significant lattice distortion in the crystal structure of WO_3 NRs grown over the rGO sheet. The SAED pattern of rGO–WO_3 composite is shown in Fig. 3(c)(iii). The SAED pattern also clearly shows two rings corresponding to the (001) and (320) planes of the tetragonal phase of WO_3, which further indicates that the WO_3 nanostructures are nicely grown over the graphene sheet. This result is well consistent with those obtained from the XRD data. The values of the inter-planar spacing, as determined by the SAED pattern, are in good agreement with those calculated using XRD data. It can also be seen from the SAED pattern, as shown in Fig. 3(b)(iii) and c(iii)], that the growth direction of WO_3 is preferably along the (140) plane in pure WO_3 NRs and along the (320) plane in case of WO_3 grown over the rGO sheet.

4.3. Raman spectroscopy

The Raman spectra of GO and rGO samples recorded in the spectral range 1000–2000 cm^{-1} are shown in Fig. 4(a). The Raman spectra of pure WO_3 NRs and rGO–WO_3 composite recorded in the spectral range 200–1800 cm^{-1} are shown in Fig. 4(b). Raman peaks are used to determine the coordination of carbon atoms in GO, rGO, and rGO–WO_3 composite. In the Raman spectra of GO, the position of D and G bands are found to be ~1354 and ~1591 cm^{-1}, respectively.[25] The G band is attributed to the first order phonon scattering of the E_{2g} mode consisting of sp^2 hybridized C–C bonds in a two-dimensional hexagonal lattice whereas the D band results from sp^3 hybridized carbon, defects, and structural imperfections in the graphite layers. Thus, the value of I_D/I_G provides information about sp^2 bonded carbons, which are mainly responsible for the formation of the 2D structure of the rGO sheet. The value of I_D/I_G is generally used to determine the defects and the fraction of sp^3/sp^2 bonded carbon atoms in the rGO sheet.[26] The value of I_D/I_G for GO and rGO turns out to be 0.87 and 1.09, respectively. The higher value of I_D/I_G in case of rGO–WO_3 composite may be due to the increase in oxygenated functional groups in the rGO sheet.[26] This result is consistent with those obtained by analyzing the XRD data.

Fig. 4(b) shows the Raman spectra of as synthesized pure WO_3 NRs and rGO–WO_3 composite. Here, it is interesting to note that WO_3 NRs behave as an excellent Raman scatterer. We observed that the intensity of the most intense peak has ~60 000 counts for an exposure time of 0.5 s only. This further indicates that the synthesized material is having good crystallinity. Four Raman bands are observed in the Raman spectrum of pure WO_3 NRs. These bands are positioned at ~263, ~318, ~709, and ~798 cm^{-1}. The Raman bands at ~263 and ~318 cm^{-1} are assigned to bending [δ(O–W–O)] modes of WO_3.[27] The value of I_{263}/I_{318} is calculated to be 2.90. The Raman bands centered at ~709 and ~798 cm^{-1} are attributed to the [ν(O–W–O)] mode of WO_3.[27] The value of I_{709}/I_{798} turns out to be 0.62. The wavenumber positions of bending modes, [δ(O–W–O)] of WO_3 NRs grown over the rGO sheet are observed at ~256 and ~314 cm^{-1}. The red shift of the wavenumber positions of bending and stretching modes of WO_3 NRs grown over the rGO sheet compared to their values in pure WO_3 NRs may be due to the interaction of WO_3 NRs with the surface of the rGO sheet. In addition to the signature of Raman bands of WO_3 NRs grown over the rGO sheet, the D and G bands have also been observed at ~1354 and ~1583 cm^{-1}, respectively in the rGO–WO_3 composite. This indicates that the WO_3 NRs have nicely been grown over the rGO sheet, which we could not confirm by analyzing the XRD data. It further suggests the formation of WO_3 NRs on the surface of rGO sheet, as reported in earlier study.[25] The values of I_D/I_G for rGO–WO_3 and rGO are calculated to be 0.90 and 1.00, respectively. The reduced value of I_D/I_G in case of rGO–WO_3 composite indicates that the number of sp^2 bonded carbon atoms is increased during the *in situ* synthesis of rGO–WO_3 composite. It means that the damaged sp^2 network is repaired in case of *in situ* synthesis of rGO–WO_3 composite. The values of I_{256}/I_{314} and I_{704}/I_{795} for rGO–WO_3 composite turn out to be the same as their values calculated for pure WO_3 NRs. This

observation suggests that the structural morphology of WO_3 NRs grown over the rGO sheets is the same in case of pure WO_3 NRs.

4.4. UV-Vis spectroscopy

Fig. 5(a) shows the UV-Vis absorption spectra of as prepared WO_3 NRs and rGO–WO_3 samples in the spectral range of 200–620 nm. From these spectra, one can see that the absorption edges are located at ~330 and ~360 nm for pure WO_3 NRs and rGO–WO_3 composite, respectively. The red shift in the value of the absorption edge in rGO–WO_3 composite may be due to the restoration of the π–π transition of the aromatic C–C bonds of rGO–WO_3 composite.[25] The band gap energy of these samples can be calculated from the absorption spectra. The following expression was used to calculate the optical band gap for pure WO_3 NRs and rGO–WO_3 composite:[28]

$$(\alpha h\nu)^n = K(h\nu - E_g)$$

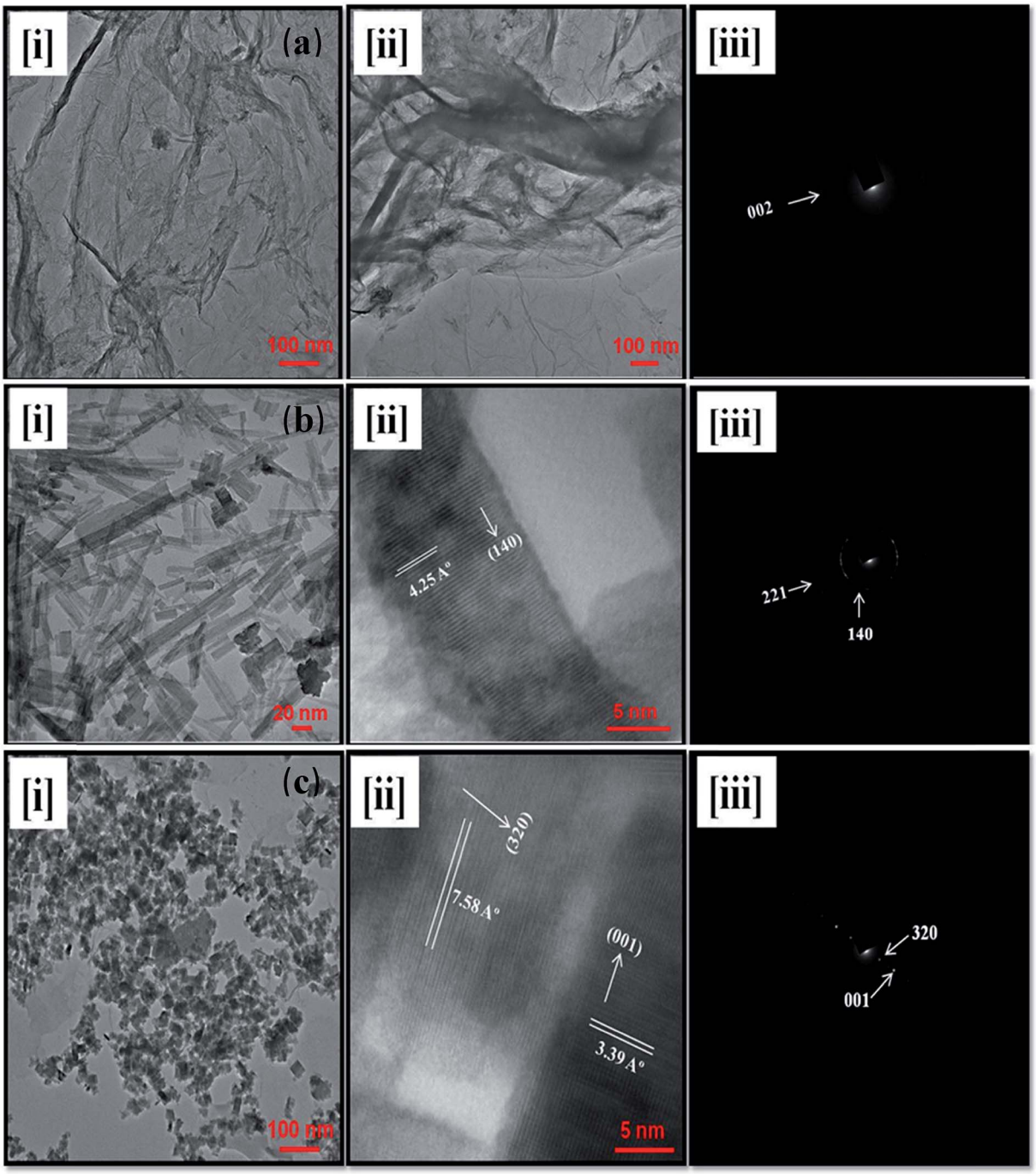

Fig. 3 TEM micrographs of rGO (a, i and ii), WO_3 NRs (b, i and ii), and rGO–WO_3 composite (c, i and ii). and SAED patterns of rGO (a, iii), WO_3 NRs (b, iii), and rGO–WO_3 composite (c, iii).

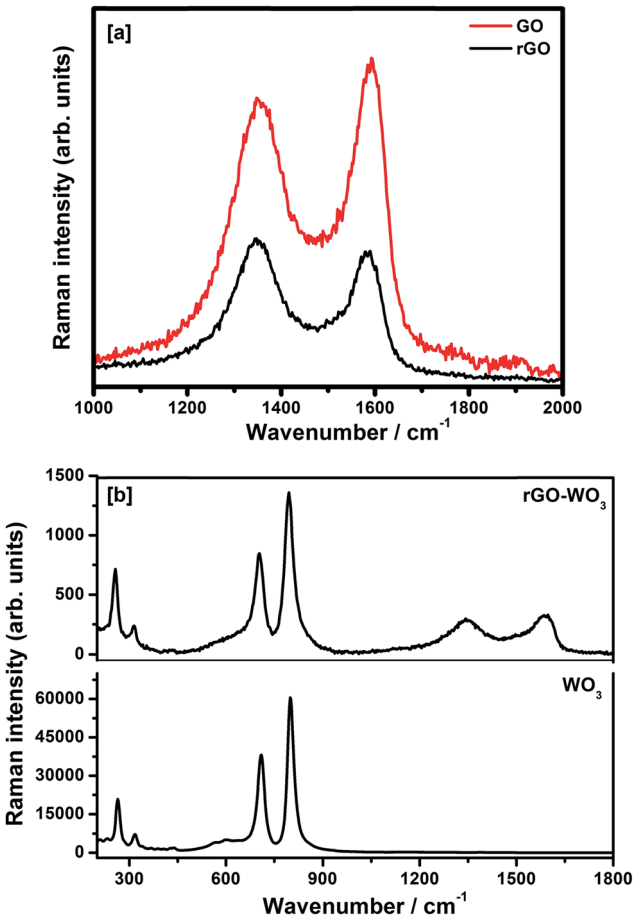

Fig. 4 Raman spectra of (a) GO and rGO, and (b) WO_3 NRs and rGO–WO_3 composite.

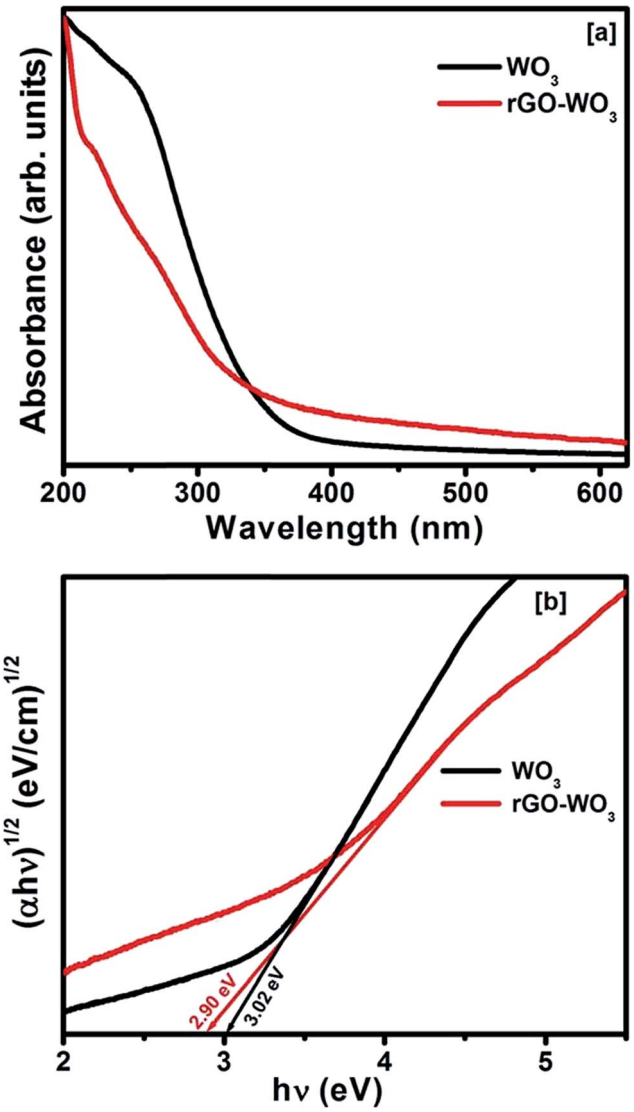

Fig. 5 (a) UV-Vis absorption spectra and [b] $(\alpha h\nu)^{1/2}$ *vs.* $h\nu$ plots for the determination of the optical band gap of WO_3 NRs and rGO–WO_3 composite.

where α, $h\nu$, E_g, and K are the absorption coefficient, incident photon energy, band gap, and a constant, respectively. The value of n is taken to be 1/2 for indirect band gap and 2 for direct band gap materials.[28] In Fig. 5(b), the linear extrapolation of the Tauc plot $[(\alpha h\nu)^{1/2}$ *vs.* $h\nu]$ intercepts the x axis at a certain point. The value of intercept with the x axis provides the value of the optical band gap. As per the intercept at x axis, the value of optical band gap is calculated to be ~3.02 and ~2.90 eV for WO_3 NRs and rGO–WO_3 composite, respectively. The reduction in the value of the band gap of rGO–WO_3 composite may be attributed to the interaction of the rGO sheets and the WO_3 NRs grown over it. It is in good agreement with the results reported in the earlier study.[25] Hence, the light absorption and emission properties of WO_3 NRs may be modified by decorating it over the rGO sheet, which may be helpful to find its applications in various fields of science and technology.

4.5. PL spectroscopy

The PL studies of material help to understand the different energy states available in the conduction (CB) and valence band (VB) and radiative transitions between these levels. It also provides information regarding energy states lying within the CB and VB. The efficiency of charge carriers trapping, transfer of electrons and holes in the semiconductors are also estimated by analyzing the PL spectra. The room temperature emission spectra of WO_3 NRs and rGO–WO_3 composite excited with different wavelengths (energies) 250 (4.96), 270 (4.59), and 280 nm (4.43 eV) are shown in Fig. 6(a and b). Fig. 6(a) shows the PL spectra of WO_3 NRs excited at 250, 270, and 280 nm. In the emission spectra of WO_3 NRs recorded at wavelengths of 250 and 270 nm, effectively three emission bands were observed, out of which one band positioned at ~423 nm is found to be the most intense. However, in the emission spectra recorded at a wavelength of 280 nm, an emission band is appeared at ~383 nm which we could not see in the spectra recorded at excitation wavelengths 250 and 280 nm. A similar emission spectra were observed for the rGO–WO_3 composite excited at wavelengths of 250, 270, and 280 nm, except for a variation in the intensity of certain bands. The position of the emission bands in the emission spectra of WO_3 NRs and rGO–WO_3

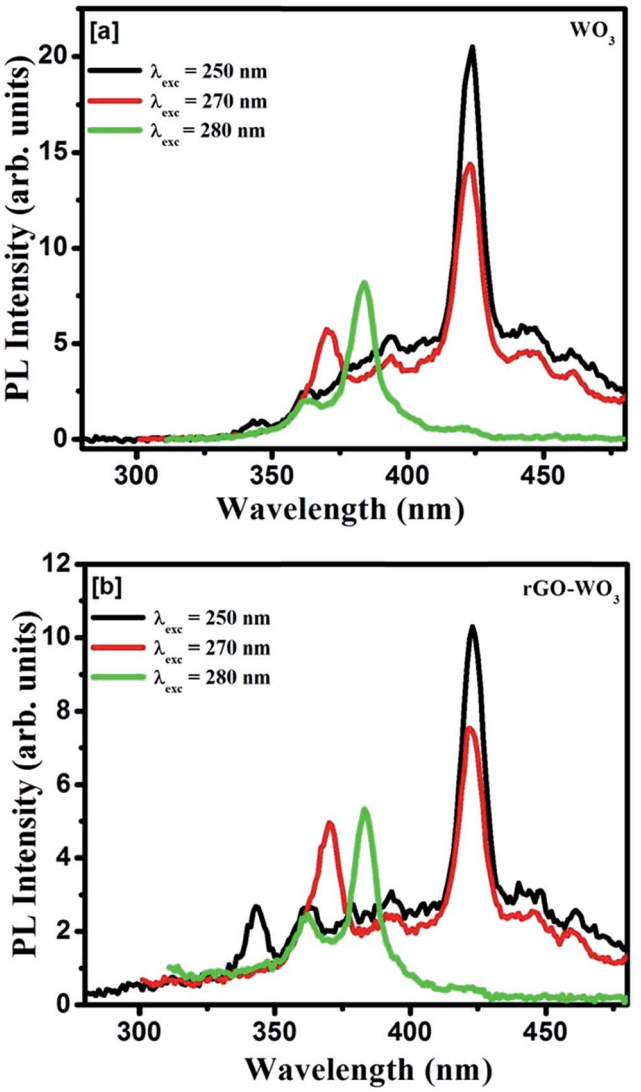

Fig. 6 PL spectra of (a) WO_3 NRs and (b) rGO–WO_3 composite samples excited at wavelengths 250, 270, and 280 nm.

composite was found to be almost the same. The decrease in intensity of the emission bands in rGO–WO_3 compared to the intensities observed for WO_3 NRs demonstrates a delay in the recombination time of electrons and holes in the rGO–WO_3 composite. This may be due to the transfer of electrons from WO_3 NRs to the rGO sheet, which essentially causes to decrease the recombination rate of electrons and holes.[15] The emission band at ~383 nm (3.23 eV) is found to be the most intense peak in the emission spectra of WO_3 NRs and rGO–WO_3 composite excited at a wavelength of 280 nm. This band may be attributed to the inter-band transition. The emission bands observed in the spectra of WO_3 NRs and rGO–WO_3 composite except the band positioned at ~423 nm may be attributed to low-lying resonant states in the CB of WO_3 NRs whereas the emission of the band centered at ~423 nm is caused by the band-to-band edge transition. The weak emission bands observed in the spectral range 440–500 nm might originate from the presence of oxygen vacancies.[29] The low intensity of these bands indicates the presence of a smaller number of oxygen vacancies in the samples. In an earlier study,[30] the emission band at ~423 nm of rGO–WO_3 composite is assigned to the near-band edge emission. The emission bands observed for rGO–WO_3 composite are nicely explained with the help of a schematic diagram as shown in Fig. 7.

4.6. Dielectric properties

4.6.1 Dielectric constant and dielectric loss. The values of the dielectric constant (ε') and dielectric loss (ε'') of pure WO_3 NRs and rGO–WO_3 composite were calculated using the following relationships:

$$\varepsilon' = \frac{Z''}{\omega C_o\left(Z'^2 + Z''^2\right)}$$

$$\varepsilon'' = \frac{Z'}{\omega C_o\left(Z'^2 + Z''^2\right)}$$

where Z' and Z'' are the real and imaginary parts of the complex impedance Z, and C_o is the capacitance of the cell. The frequency dependences of ε' and ε'' of WO_3 NRs and rGO–WO_3 composite calculated in the frequency range 2.5–6.0 (logarithmic scale) are shown in Fig. 8(a) and (b), respectively. The value of the dielectric constant of WO_3 NRs and rGO–WO_3 composite is decreased with increasing frequency. Here, we would like to note that initially (up to frequency 3.5 Hz), the value of the dielectric constant of rGO–WO_3 composite is higher than that of the pure WO_3 NRs and after 3.5 Hz, the value is found to be relatively smaller compared to WO_3 NRs. The increased value of the dielectric constant of the rGO–WO_3 composite compared to WO_3 NRs in the lower-frequency range clearly demonstrates that the value of ε' of rGO–WO_3 is enhanced in the presence of rGO sheet. At lower frequencies, the relatively large value ε' for rGO–WO_3 composite may be explained in terms of polarization induced new dipoles, which

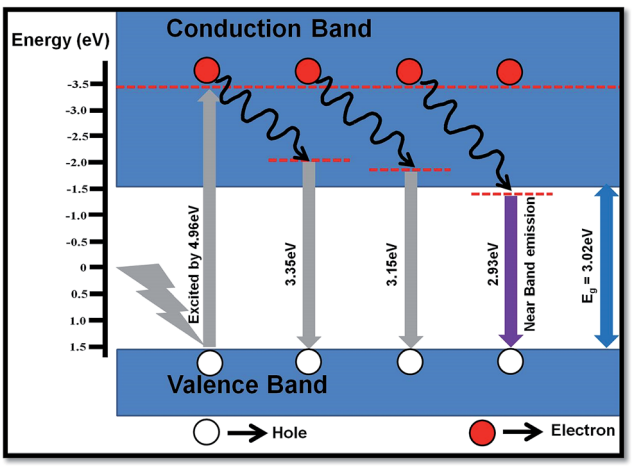

Fig. 7 Schematic of different possible transitions in the rGO–WO_3 composite excited at a wavelength of 250 nm.

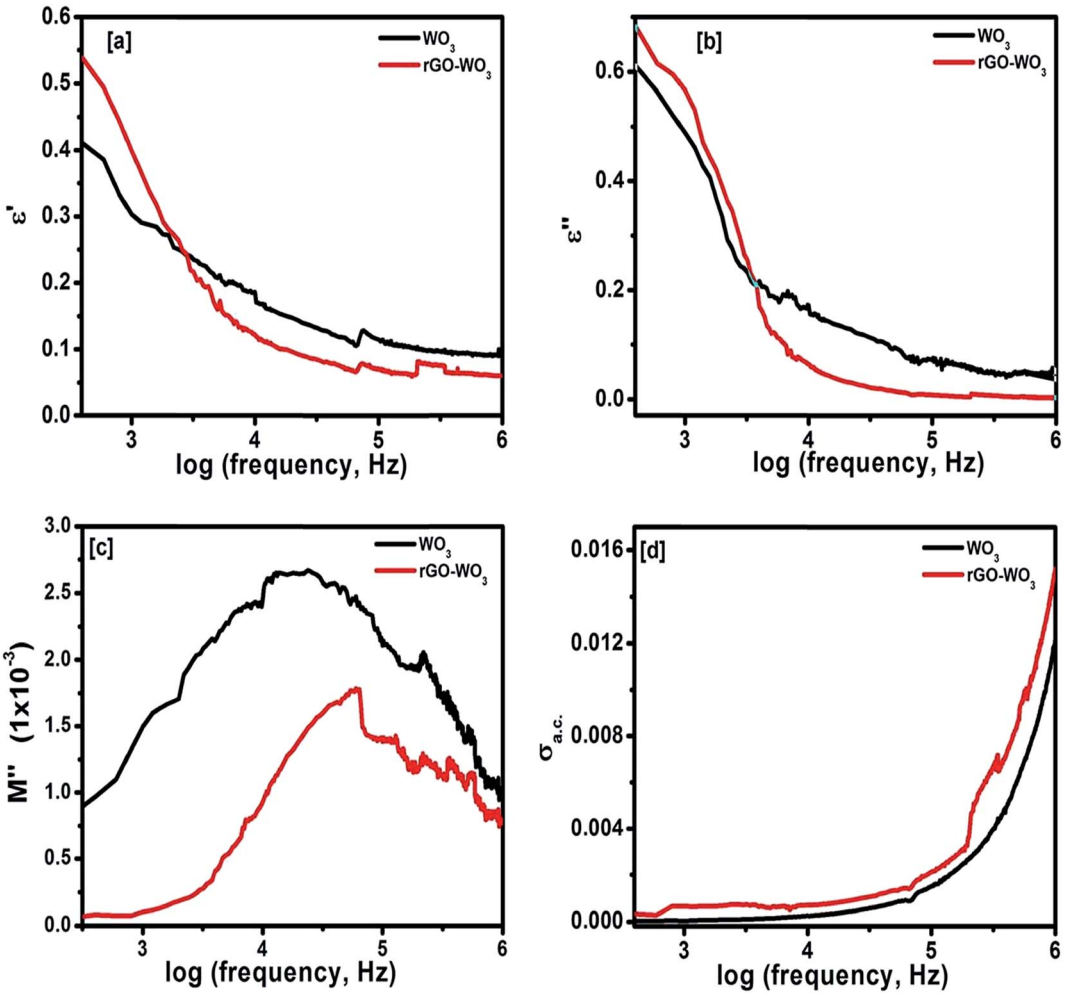

Fig. 8 Frequency dependence of (a) dielectric constant, (b) dielectric loss, (c) imaginary part of electric modulus, and (d) ac conductivity of WO_3 NRs and rGO–WO_3 composite.

initially follow the applied field and causes to enhance the value of ε'. It could also be due to the blocking of charge carriers at the interface. The spatial polarization arising from the trap states results an accumulation of charge carriers and leading to an increase of the value of ε'.

The overall decrease in the value of dielectric constant of the WO_3 NRs and rGO–WO_3 composite with increase of frequency could be due to the induced polarization process, which essentially does not follow the changes in ac frequency rapidly and causes to decrease its value gradually with increase of frequency.[31] The occurrence of the polarization process in WO_3 NRs and rGO–WO_3 composite may be due to the existence of a large number of trap states at the grain boundaries of the synthesized samples. These trap states are generated due to the presence of defects/vacancies such as, oxygen vacancies, dangling bonds, micro porosities *etc.* These trap states can induce charges with different time constants. At higher frequencies, the induced charges can no longer be able to rotate with a sufficient speed and, therefore, their frequency lags behind the applied ac signal, resulting decrease in the value of ε'.[32] Here, it is worthy to note that the rate of decrease in ε' in rGO–WO_3 composite is relatively smaller compared to WO_3 NRs. It further supports the fact that the polarization process in WO_3 NRs is enhanced in presence of the rGO sheet, which also does not follow the applied electric field.

The dielectric loss (ε'') describes the energy dissipation in the material *via* transport-related loss (conduction loss), dipolar loss, and interfacial polarization contribution.[33] For the rGO–WO_3 composite, the dielectric loss can be presented by the following expression:[34]

$$\varepsilon'' = \varepsilon''_{dc} + \varepsilon''_{MW} + \varepsilon''_{D}$$

where, ε''_{dc}, ε''_{MW} and ε''_{D} are related to the conduction loss, interfacial polarization loss, and dipole loss factor, respectively. The conduction loss, ε''_{dc} and interfacial polarization loss, ε''_{MW} in a composite dielectric material are estimated by the following relationship:[34]

$$\varepsilon''_{dc} = \frac{\sigma_{dc}}{2\pi f}$$

where σ_{dc} and f represent the direct current conductivity and frequency, respectively,[34] and:

$$\varepsilon''_{MW} \propto \frac{K}{1+(2\pi f)^2\tau^2}$$

where K is related to the dielectric constant of the pellets at the interface and τ is the relaxation time of the interfacial polarization.

Fig. 8(b) shows the dependence of ε'' for the WO_3 NRs and rGO–WO_3 composite as function of the logarithm of the frequency. From Fig. 8(b), it appears that the value of ε'' for both WO_3 NRs and rGO–WO_3 composite is decreased with increasing frequency. In general, the high frequency process is associated with dipolar relaxation whereas, at lower frequency, the contribution of the interfacial polarization and conductivity in the material is considered to be more significant. Similar to the variation of ε' at lower frequency, the value of ε'' is also higher in case of rGO–WO_3 composite than that of WO_3 NRs. This further indicates that more energy is being utilized to induce polarization and dipoles in rGO–WO_3 composite at lower frequency compared to WO_3 NRs. Further, at higher frequency, the rate of dielectric loss in rGO–WO_3 composite is relatively smaller compared to WO_3 NRs. This indicates that at higher frequency, the induced polarization and dipoles do not follow the applied field, resulting in a decrease in dielectric loss at higher frequency. In order to understand the complete dielectric response of the synthesized products, a quantity called "dielectric modulus" is introduced. It provides information about the interfacial mechanism of the synthesized samples as function of frequency of the applied field. The dielectric modulus (M^*) is defined by the following expression:[34]

$$M^* = \frac{1}{\varepsilon^*} = \frac{1}{\varepsilon' - j\varepsilon''} = \frac{\varepsilon'}{\varepsilon'^2 - j\varepsilon''^2} + j\frac{\varepsilon''}{\varepsilon'^2+\varepsilon''^2} = M' + jM''$$

here, M'' represents the dielectric loss, which helps us to explain the relaxation phenomena. In the previous studies,[35,36] the dielectric modulus has been used to understand the interfacial polarization of the nanostructured materials.[35,36] The calculated values of M'' for WO_3 NRs and rGO–WO_3 composite were plotted as function of the applied frequency and the plot is shown in Fig. 8(c). In both the plots, the variation of M'' with frequency shows a similar type of trend, *i.e.* the value of M'' is increased with increase of frequency and after reaching to a maximum value at certain frequency, it starts to decrease, *i.e.* both the curves show a peaking behavior. The rising part of the curve at lower frequency represents the interfacial polarization and the maximum of the curve at certain frequency yields the maximum interfacial polarization at that frequency. In case of rGO–WO_3 composite, this peak shifts towards the higher frequency side compared to the position observed for pure WO_3 NRs. The up-shift in peak position for rGO–WO_3 in the frequency spectrum describes the enhancement of interfacial polarization.[35,36] Thus, it is worthy to note that the interfacial polarization in WO_3 NRs is enhanced in the presence of the rGO sheet. The enhancement in interfacial polarization in composite materials had also been reported in previous study[34] for ZnO grown over the rGO sheet. The enhancement in interfacial polarization may be due to the accumulation of charge at the interface of WO_3 and the rGO sheet.

4.6.2 AC electrical conductivity. The ac conductivity of the dielectric materials can be defined by the following relation:[37]

$$\sigma(\omega) = \sigma'(\omega) + \sigma''(\omega)$$

where $\sigma'(\omega)$ is the real part ($2\pi f\varepsilon'\varepsilon''$) and $\sigma''(\omega)$ is the imaginary part ($2\pi\varepsilon_o\varepsilon'$).

The frequency dependence of the ac conductivity (σ_{ac}) of the synthesized materials calculated at room temperature is shown in Fig. 8(d). By looking at Fig. 8(d), one can easily notice that the ac conductivity in WO_3 NRs and rGO–WO_3 composite materials shows a strong dependence on the frequency of the applied field. The increase in ac conductivity with frequency is governed by the following relationship:[37]

$$\sigma(\omega) = A\omega^n$$

where ω is the angular frequency of the ac signal, A is the proportionality constant and n is the temperature dependent parameter having a value less than 1 at room temperature. In both the materials, the value of the ac conductivity is increased almost exponentially with increase in frequency. The rate of increase in ac conductivity at lower frequency is quite small compared to that of found at higher frequency. As the value of the logarithm of the frequency becomes $\geq$5, the conductivity in WO_3 NRs and rGO–WO_3 composite increases rapidly. The value of the ac conductivity in the rGO–WO_3 composite over the entire frequency range is relatively greater compared to the value found for pure WO_3 NRs. Different conduction mechanisms such as hopping, tunneling, or free band conduction may lead to the observed behavior of the ac conductivity (σ_{ac}). From our results, it is difficult to determine which mechanism is responsible for inducing the conduction properties in the synthesized samples. However, in case of the rGO–WO_3 composite, the rGO sheet may make a long-range connectivity through attached oxygenated functional group to the WO_3 NRs. This phenomenon is called percolation and the minimum volume fraction of fillers, which can make the percolation form at the interface, is named percolation threshold.[38] The effect of the filler shape on the threshold value is significant for the ac conductivity in the material. Dang *et al.*[39] had reported a percolation threshold value of 50–70 vol% for spherical ceramic fillers. Li *et al.*[40] had also reported a percolation threshold of 2.4 wt% for a PVDF/graphite nano-platelet composite. The value of the logarithm of the frequency, where the ac conductivity of WO_3 NRs and rGO–WO_3 composite can be used to reflect the threshold value, is measured to be 4.90 Hz. As shown in Fig. 8(d), near the percolation threshold, the ac conductivities of WO_3 NRs and rGO–WO_3 composite at a value of log(frequency) = 3 are calculated to be $\sim 5.7 \times 10^{-5}$ and $\sim 6.9 \times 10^{-4}$ S m^{-1}, respectively. At log(frequency) = 5.3, these values are calculated to be $\sim 2.6 \times 10^{-3}$ and $\sim 3.6 \times 10^{-3}$ S m^{-1}, respectively. It confirms that the rGO sheet has a sp^2 network and restores the conductivity partially in the rGO–WO_3 composite compared to pure WO_3 NRs. The electrical properties of GO may be controlled by adjusting the oxidation states as discussed by Wang *et al.*[41] Therefore, it can be expected that the

ac conductivity of WO_3 NRs will also be controlled by introducing a graphene matrix.

5. Conclusions

In summary, a controlled synthesis of pure WO_3 NRs and rGO–WO_3 composite is performed using a simple one-step hydrothermal method. The synthesized samples were characterized by XRD, TEM, Raman, UV-Vis, and PL spectroscopy. XRD revealed orthorhombic and tetragonal phases of pure WO_3 NRs and rGO–WO_3 composite, respectively. TEM and Raman spectroscopy measurements confirmed the formation of WO_3 NRs over the rGO sheet. The intensity ratio of Raman bands clearly revealed that the structural morphology of WO_3 NRs in rGO–WO_3 composite is the same as that of pure WO_3 NRs. The low intensity of the emission bands in rGO–WO_3 composite may be due to the transfer of electrons from WO_3 NRs to the rGO sheet. The dielectric properties of WO_3 NRs and rGO–WO_3 composite were studied. At lower frequency, rGO–WO_3 composite shows larger dielectric constant compared to pure WO_3 NRs, which could be due to the potential barrier formed by the trap states arising from the spatial polarization at the interface. At higher frequencies, the dielectric constant is decreased in both, pure WO_3 NRs and rGO–WO_3 composite. At higher frequency, the induced dipoles no longer be able to rotate with sufficient speed and therefore their oscillation lags behind the applied ac signal, resulting decrease in the value of dielectric constant. The interfacial polarization in WO_3 NRs is enhanced significantly in the presence of the rGO sheet. The enhancement in interfacial polarization may be due to the accumulation of charges at the interface. An enhancement in ac conductivity has also been observed in case of WO_3 NRs grown over the rGO sheet. It may be due to the long range connectivity of WO_3 NRs with the rGO sheet *via* oxygenated functional groups attached to the rGO sheet. The higher number of sp^2 carbon bonds in the rGO sheet may also be responsible for the enhanced value of the ac conductivity in the rGO–WO_3 composite.

Acknowledgements

BA and AKO are thankful to the Department of Science and Technology (DST), New Delhi for providing the financial support through research grant SR/FTP/PS-038/2011 and AvH foundation for providing the financial support to visit Jacobs University Bremen, Germany. AKO is thankful to the DFG (Deutsche Forschungsgemeinschaft), Germany for financial support of his visit to the research group of Prof. Ingo Fischer, Institute of Physical Chemistry, Wuerzburg, Germany for three months under contract Fi575/12-1, "Initiation of Bilateral Cooperations". Authors are thankful to Centre for Interdisciplinary Research, Motilal Nehru National Institute of technology Allahabad for providing the XRD facility.

References

1 M. E. Lines and A. M. Glass, *Principles and Applications of Ferroelectrics and Related Materials*, Oxford, New York, 1997.
2 R. Ubic and I. M. Reany, Structure and Dielectric Properties of Lead Pyrochlores, *J. Am. Ceram. Soc.*, 2002, **85**, 2472–2478.
3 Q. M. Zhang, H. F. Li, M. Poh, F. Xia, Z. Y. Cheng, H. Xu and C. Huang, An all –organic composite actuator material with a high dielectric constant, *Nature*, 2002, **419**, 284–287.
4 Y. Wu, X. Shen, X. Shen, X. Sun, X. Liu, Z. Wang and J.-K. Kim, Exceptional dielectric properties of chlorine-doped graphene oxide/poly (vinylidene fluoride) nanocomposites, *Carbon*, 2015, **89**, 102–112.
5 N. Yousefi, X. Sun, X. Lin, X. Shen, J. Jia, B. Zhang, B. Tang, M. Chan and J.-K. Kim, Highly aligned graphene/polymer nanocomposites with excellent dielectric properties for high performance electromagnetic interference shielding, *Adv. Mater.*, 2014, **26**, 5480–5487.
6 Y. Huang, J. Liang and Y. Chen, The application for graphene based materials for actuators, *J. Mater. Chem.*, 2012, **22**, 3671–3679.
7 S. Guo and S. Dong, Graphene nanosheets: synthesis, molecular engineering, thin films, hybrids, and energy and analytical applications, *Chem. Soc. Rev.*, 2012, **40**, 2644–2672.
8 S. Stankovich, D. A. Dikin, R. D. Piner, K. A. Kohlhaas, A. Kleinhammes, Y. Jia, Y. Wu, S. T. Nguyen and R. S. Ruof, Synthesis of graphene-based nanosheets *via* chemical reduction of exfoliated graphite oxide, *Carbon*, 2007, **45**, 1558–1565.
9 S. Mao, H. H. Pu and J. Chen, Graphene oxide and its reduction: modelling and experimental progress, *RSC Adv.*, 2012, **2**, 2643–2662.
10 A. K. Geim and K. S. Novoselov, The rise of graphene, *Nat. Mater.*, 2007, **6**, 183–191.
11 K. Ahmad, W. Pan and S. L. Shi, Electrical conductivity and dielectric properties of multiwalled carbon nanotube alumina composites, *Appl. Phys. Lett.*, 2006, **89**, 133122.
12 C. Wu, X. Huang, L. Xie, X. Wu, J. Yu and P. Jiang, Morphology controllable graphene TiO_2 nanorod hybrid nanostructures for polymer composites with high dielectric performance, *J. Mater. Chem.*, 2011, **21**, 17729–17736.
13 R. K. Jammula, A. Tumuluri, N. K. Rotte, K. C. J. Raju and V. V. S. S. Srikanth, Cupric oxide decked few layered graphene: synthesis and dielectric behaviour, *Carbon*, 2014, **78**, 374–383.
14 J. Chang, M. J. F. Yao, T. H. Kim, V. T. Le, H. Yue, F. Gunes, B. Li, A. Ghosh, S. Xie and Y. H. Lee, Asymmetric supercapacitors based on graphene/MnO_2 nanospheres and graphene/MoO_3 nanosheets with high energy density, *Adv. Funct. Mater.*, 2013, **13**, 5074–5083.
15 J. Guo, Y. Li, S. Zhu, Z. Chen, Q. Liu, D. Zhang, W. J. Moon and D. M. Song, Synthesis of WO_3@graphene composite for enhanced photocatalytic oxygen evolution from water, *RSC Adv.*, 2012, **2**, 1356–1363.
16 A. Subrahmanyam and A. Karuppasamy, Optical and electrochromic properties of oxygen sputtered tungsten oxide (WO_3) thin films, *Sol. Energy Mater. Sol. Cells*, 2007, **91**, 266–274.
17 S. Balaji, Y. Djaoued, A. S. Albert, R. Bruning, N. Beaudoin and J. Robichaud, Porous orthorhombic tungsten oxide thin films: synthesis, characterization and application in

electrochromic and photochromic devices, *J. Mater. Chem.*, 2011, **21**, 3940–3948.

18 J. Zhang, X. L. Wang, X. H. Xia, C. D. Gu, Z. J. Zhao and J. P. Tu, Enhanced electrochromic performance of macroporous WO_3 films formed by anodic oxidation of DC sputtered tungsten layers, *Electrochim. Acta*, 2010, **55**, 6953–6958.

19 M. T. Chang, L. J. Chou, Y. L. Chueh, Y. C. Lee, C. H. Hsieh, C. D. Chen, Y. W. Lan and L. J. Chen, Nitrogen doped tungsten oxide nanowires: low temperature synthesis on Si, and electrical, optical, and field emission properties, *Small*, 2007, **3**, 658–664.

20 Y. He, Z. Wu, L. Fu, C. Li, Y. Miao, L. Cao, H. Fan and B. Zou, Photochromism and size effect of WO_3–TiO_2 aqueous Sol, *Chem. Mater.*, 2003, **15**, 4039–4045.

21 D. M. Satoca, L. Borja, A. Rodes, R. Gomez and P. Salvador, Photoelectrochemical behaviour of nanostructured WO_3 thin films electrodes: the oxidation of formic acid, *ChemPhysChem*, 2006, **7**, 2540–2551.

22 E. L. Miller, B. Marsen, B. Cole and M. Lum, Low temperature reactively sputtered tungsten oxide films for solar powered water splitting applications, *Electrochem. Solid-State Lett.*, 2006, **9**, G248–G250.

23 T. Hirose and K. Furukawa, Dielectric anomaly of tungsten trioxide WO_3 with giant dielectric constant, *Phys. Status Solidi A*, 2006, **203**, 608–615.

24 Z. Bo, X. Shuai, S. Mao, H. Yang, J. Qian, J. Chen, J. Yan and K. Cen, Green preparation of reduced graphene oxide for sensing and energy storage applications, *Sci. Rep.*, 2014, **4**, 4684.

25 L. Fu, T. Xia, Y. Zheng, J. Yang, A. Wang and Z. Wang, Preparation of WO_3-reduced graphene oxide nanocomposites with enhanced photocatalytic property, *Ceram. Int.*, 2015, **41**, 5903–5908.

26 V. Chandra, J. Park, Y. Chun, J. W. Lee, I. C. Hwang and K. S. Kim, Water dispersible magnetite reduced graphene oxide composites for arsenic removal, *ACS Nano*, 2010, **4**, 3979–3986.

27 B. Ahmed, S. Kumar, A. K. Ojha, P. Donfack and A. Materny, Facile and controlled synthesis of aligned WO_3 nanorods and nanosheets as an efficient photocatalysis material, *Spectrochim. Acta, Part A*, 2017, **175**, 250–261.

28 D. Chen, L. Gao, A. Yasumori, K. Kuroda and Y. Sugahara, Size and shape controlled conversion of tungstate based Inorganic organic hybrid belts to WO_3nanoplates with highspecific surface areas, *Small*, 2008, **10**, 1813–1822.

29 J. Y. Luo, F. L. Zhao, L. Gong, H. J. Chen, J. Zhou, Z. L. Li, S. Z. Deng and N. S. Xu, Ultraviolet-visible emission from three-dimensional WO_{3-x} nanowire networks, *Appl. Phys. Lett.*, 2007, **91**, 093124.

30 F. Zheng, M. Guo and M. Zhang, Hydrothermal preparation and optical properties of orientation controlled WO_3 nanorod arrays on ITO substrates, *CrystEngComm*, 2013, **15**, 277–284.

31 K. C. Kao, *Dielectric phenomena in solids*, Academic Press Inc. 2004.

32 H. M. Chenari, M. M. Golzan, H. Sedghi, A. Hassanzadeh and M. Talebian, Frequency dependence of dielectric properties and electrical conductivity of Cu/nano-SnO_2 thick film/Cu arrangement, *Curr. Appl. Phys.*, 2011, **11**, 1071–1076.

33 L. Xie, X. Huang, C. Wu and P. Jiang, Core–shell structured poly (methyl methacrylate)/$BaTiO_3$ nanocomposites prepared by *in situ* atom transfer radical polymerization: a route to high dielectric constant materials with the inherent low loss of the base polymer, *J. Mater. Chem.*, 2011, **21**, 5897–5906.

34 Y. Feng, W. L. Li, Y. F. Hou, Y. Yu, W. P. Cao, T. D. Zhang and W. D. Fei, Enhanced dielectric properties of PVDF-HFP/$BaTiO_3$-nanowires composites induced by interfacial polarization and wire shape, *J. Mater. Chem. C*, 2015, **3**, 1250–1260.

35 M. Laurati, P. Sotta, D. R. Long, L. A. Fillot, A. Arbe, A. Alegria, J. P. Embs, T. Unruh, G. J. Schneider and J. Colmemero, Dynamics of water absorbed in polyamides, *Macromolecules*, 2012, **45**, 1676–1687.

36 G. M. Tsagaris, G. C. Psarras and N. Kouloumbi, Electric modulus and interfacial polarization in composite polymetric systems, *J. Mater. Sci.*, 1998, **33**, 2027–2037.

37 J. C. Dyre and T. B. Schroder, Universality of ac conduction in disordered solids, *Rev. Mod. Phys.*, 2000, **72**, 873–892.

38 G. S. Wang, Enhanced dielectric properties of three phase percolative composites based on thermoplastic ceramic matrix ($BaTiO_3$ + PVDF) and ZnO radial nanostructures, *ACS Appl. Mater. Interfaces*, 2010, **2**, 1290–1293.

39 Z. M. Dang, T. Zhou, S. H. Yao, J. K. Yuan, J. W. Zha, H. T. Song, J. Y. Li, Q. Chen, W. T. Yang and J. Bai, Advanced calcium copper titanate/polyimide functional hybrid films with high dielectric permittivity, *Adv. Mater.*, 2009, **21**, 2077–2082.

40 Y. C. Li, S. C. Tjong and R. K. Y. Li, Electrical conductivity and dielectric response of poly (vinylidene fluoride) graphite nanoplatelet composites, *Synth. Met.*, 2010, **160**, 1912–1919.

41 Z. Wang, J. K. Nelson, H. Hillborg, S. Zhao and L. S. Schalder, Graphene oxide filled nanocomposites with novel electrical and dielectric properties, *Adv. Mater.*, 2012, **24**, 3134–3137.

